

FINAL DRAFT GT2008-50328

INVESTIGATING CIRCUMFERENTIAL NON-UNIFORMITIES IN THROUGHFLOW CALCULATIONS USING AN HARMONIC RECONSTRUCTION

JP. Thomas

FNRS Research Fellow
University of Liège
Turbomachinery Group
Chemin des Chevreuils 1
B-4000 Liège, Belgium
Email: jp.thomas@ulg.ac.be

O. Léonard

Professor
University of Liège
Turbomachinery Group
Chemin des Chevreuils 1
B-4000 Liège, Belgium
Email: o.leonard@ulg.ac.be

ABSTRACT

The computation time and the extraction of useful information remain severe drawbacks to systematic use of modern three-dimensional Navier-Stokes codes in a design procedure of multi-stage turbomachines. That explains why throughflow simulation is still widely used at industrial scale. The main limitation of throughflow is however the need for empirical models to reproduce blade-flow interactions and major 3D flow features.

The purpose of this work is to investigate the degree to which empiricism could be reduced by using the averaged-passage equations of Adamczyk, combined with an harmonic closure strategy. To that aim, results of a computation performed with a steady three-dimensional Navier-Stokes code are used to calculate some of the additional terms of the circumferentially-averaged equations, the so-called circumferential stresses. The importance of the latter to bring back the mean effect of circumferential non-uniformities is proven by injecting them into a throughflow simulation. The frequency spectrum of these terms is next investigated and it is demonstrated that an harmonic reconstruction can model the circumferential stresses.

NOMENCLATURE

b blockage factor
e energy source term
E total energy

f	blade force
k	kinetic energy of circumferential perturbations
le,te	leading and trailing edges
N	number of blades
P	static pressure
q	heat flux
r	radial direction
R	air specific gas constant = 287.43 J/kg.K
s	entropy (relative to inlet conditions)
T	static temperature
V	absolute velocity
y ⁺	dimensionless wall distance
z	axial direction

Greek symbols

γ	specific heat ratio = 1.4
$\delta_{i,j}$	Kronecker delta
θ	circumferential direction
ρ	density
$\tau_{i,j}$	viscous stress

Subscripts

- b inviscid
- i components in r, θ, z directions
- j components in r, z directions
- p pressure side
- s suction side
- v viscous

Superscripts

- circumferential area average
- ~ circumferential density average
- ' perturbation to circumferential area average
- " perturbation to circumferential density average
- vector

INTRODUCTION

Today it is still impossible to solve directly the Navier-Stokes equations to simulate turbulent flows in turbomachines, characterized by high Reynolds numbers. It is however established that models describing an averaged state can be successfully used to design such systems or to analyze their aerodynamic performances. In compensation, the price to pay to use these models is to add the missing information by resorting to empirical relations.

For external flows the Reynolds-Averaged Navier-Stokes equations (RANS) describe a steady state provided that the boundary conditions are steady. In this case a turbulence model is used to close the system of equations by giving a picture of the additional terms, the Reynolds stresses.

In multistage turbomachines, due to the relative movement of the rows, the RANS model is associated to an unsteady flow state characterized by disturbances of which ranges of time and length scales are very wide, leading to very long times of computation.

As an alternative, Adamczyk proposed in [1] three averaging operators (ensemble, time and passage) that lead to the well-known average-passage model, linking the unsteady turbulent flow field to a steady flow field in a typical blade passage. As it is described in [2], these operators are associated to different levels of modelisation, each one involving additional terms. The RANS equations, the time-averaged equations and the average-passage equations in particular need respectively the Reynolds stresses, the deterministic stresses and the passage-to-passage stresses to bring back the mean effects of turbulence, unsteadiness and aperiodicity on the mean steady periodic flow.

In the past few years, the closure problem has been a rich subject of research. Among all models, the harmonic closure proposed by He and Ning [3] revealed superior to the others. This method consists in solving a linearized perturbation system in the frequency domain and its efficiency to approximate

the so-called deterministic stresses has been illustrated by several authors (Chen [4], Stridh [5], Vilmin [6]). In the same way, Hall [7] developed the harmonic balance technique, which solves the non-linear RANS set of equations in the frequency domain.

In the modelisation hierarchy the throughflow model comes next, resulting from a fourth averaging, a circumferential one. Circumferential stresses appear in addition to the body forces and the energy source terms. It has been proven that these terms play an important role in the description of the flow [8]- [11], in particular on the radial pressure gradients and the entropy generation. Further investigations have highlighted the role of the circumferential stresses in a two-dimensional simulation by injecting them into a throughflow calculation [12]. The circumferential stresses were demonstrated to be at least as important as deterministic stresses and to allow the reproduction of the averaged 3D flow features, such as the corner stall or the radial mixing close to the endwalls.

In classical throughflows, these averaged 3D flow features are partly taken into account by empirical models [13]- [16]. The quality of the prediction relies then on experimental data. If it is acceptable for well-known geometries and nominal conditions, the need for more general modelisation appears in case of off-design conditions or innovating blade geometry. Therefore a transposition of the efficient harmonic closure to the circumferential stresses modelisation could be envisaged. As a first step in this direction, it is proposed here to investigate the nature of the circumferential non-uniformities in the aim of an harmonic reconstruction.

The test case used and the computation are described in the next section. It is a blade-to-blade simulation of a low speed compressor stage, at mid-span, using a mixing plane technique.

The second section is dedicated to the circumferentially-averaged representation of the flow, the extraction of the deterministic stresses and their injection into a throughflow simulation tool to illustrate the importance of these additional terms.

In the last section it is proceeded to the spectral analysis of the blade-to-blade flow field, the harmonic reconstruction of the conservative variables and the consequence on the circumferential stresses description. In particular the capability of these approximated terms to accurately reproduce the 3D-averaged flow field is illustrated.

THE TEST CASE

A viscous simulation is performed, completed by an inviscid one. The comparison of these two computations will teach the impact of the viscosity on the circumferential stresses and on their harmonic reconstruction.

For simplicity of data extraction and analysis, both calculations are performed in the blade-to-blade plane. This reduction of the problem implies the absence of secondary flow which is a source of circumferential non-uniformities. Nevertheless, it does

not introduce a lack of generality for two reasons. First, it has been demonstrated that circumferential non-uniformities in the core-flow are far from being negligible [10]- [12]. Second, the frequency behavior of a core flow is not fundamentally different from a 3D flow, as potential and viscous effects are also present.

Both computations are performed with the mixing plane technique. This implies that unsteady interactions between rows are not considered. In other words, according to the Adamczyk's model, it means that deterministic stresses are set to zero. By doing so the comparison between the blade-to-blade flow and its average will give the pure circumferential stresses associated to each row.

The cascade single stage test case

The CME2 is a single stage low speed compressor. Its global performances under nominal conditions are presented in table 1. The computation performed here concerns the mid-span section and is run under off-design conditions, near the peak efficiency, to highlight the circumferential non-uniformities. This operating point was preferred to the peak pressure point (near stall) because the latter would have involved too much disorganization and unsteadiness to allow general conclusions. For the inviscid simulation, the mass flow is imposed equal to the one obtained for the Navier-Stokes computation, in order to facilitate comparison between both calculations. The associated computed performances are listed in table 1.

	Full stage (experimental)	Mid-span section	
		viscous	inviscid
mass flow	11 kg/s	-	-
pressure ratio	1.14	1.151	1.16
efficiency	0.92	0.956	-
rotation speed	6300 RPM	6300 RPM	6300 RPM

Table 1. Global parameters of the CME2 compressor

The mesh used for the blade-to-blade viscous simulation is illustrated on the figure 1. It is composed of 74.650 grid points. An O-grid was used around the blades for a good control of the stretching in the direction normal to the wall. The spacing for the first blade cells was specified so that $y^+ < 1$ was obtained for the converged solution. The mesh used for the Euler computation involves 29.926 points.

The simulation tool

The commercial simulation tool is the structured-mesh turbomachinery code developed by Numeca. For our purpose, the steady Reynolds-Averaged Navier-Stokes equations are con-

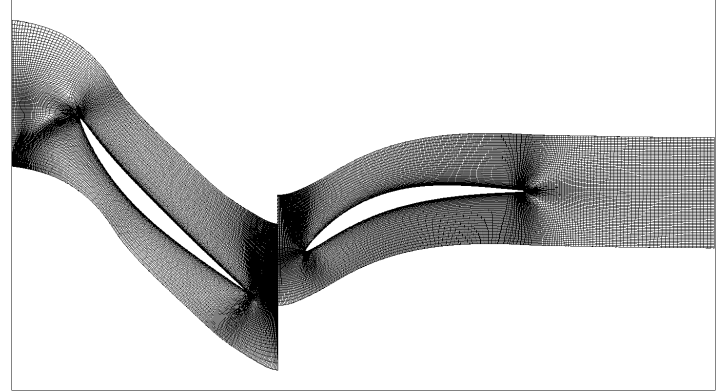


Figure 1. Blade-to-blade mesh of the mid-span section

sidered. The numerical method is based on an explicit time-marching cell-centered finite-volume approach.

The turbulence model used for this computation is the Spalart-Allmaras model.

Results of the simulation

The relative Mach number contours are depicted on figure 2 for the viscous and inviscid computations. This picture illustrates the potential effect before the leading edge, the accelerations on suction sides and, for the Navier-Stokes simulation, the wakes.

Inevitably, since the mixing-plane technique is used, the rows are nearly isolated ones, but presenting one stage of compressor is a convenient way to ensure some generality, by treating two rows with different characteristics (turning, loading...).

THE THROUGHFLOW REPRESENTATION

The aim of this section is to describe the contribution of the circumferential stresses to the throughflow description. To that end the stresses are extracted from the blade-to-blade results. These terms are next injected into the throughflow simulation, together with the viscous and inviscid blade forces and energy source terms. This section starts with the description of a fourth averaging, the circumferential one.

The circumferential averaging

There are two ways of defining the circumferential average: by using a gate function¹ or by performing an integration from the pressure side p to the suction side s . As both methods give the same result, the second one is considered here.

¹In the same way as the time-average defined by Adamczyk

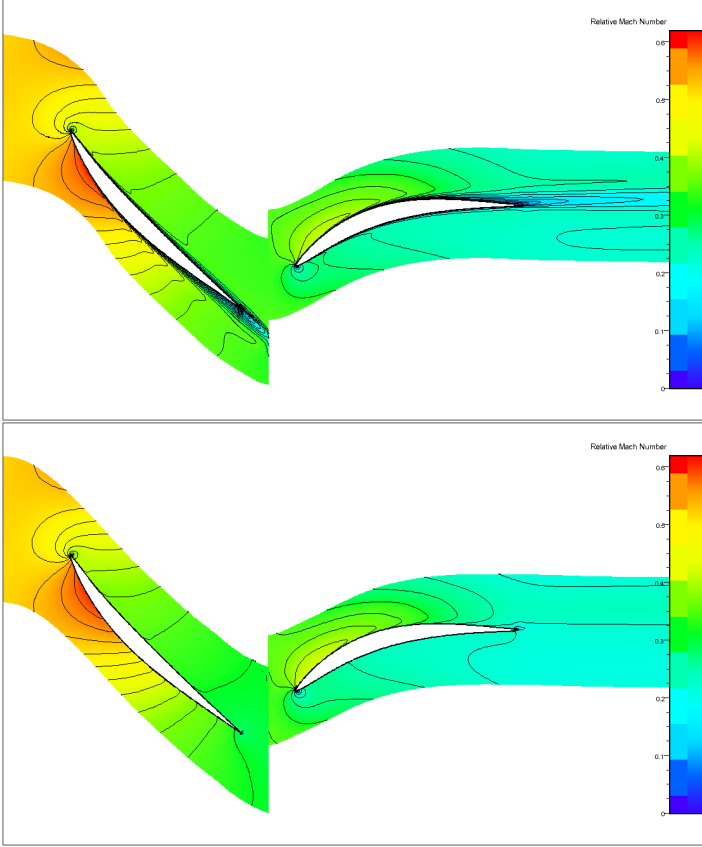


Figure 2. Relative Mach number contours: viscous (top) and inviscid (bottom)

The average of some flow variable ϕ is defined as follows:

$$\bar{\phi} = \frac{1}{\Delta\theta} \int_p^s \phi \, d\theta \quad (1)$$

where $\Delta\theta$ is equal to the azimuthal width of the blade passage. Defining the blockage coefficient b as the ratio of circumferential width occupied by the fluid over the total circumference, relation (2) is obtained.

$$\bar{\phi} = \frac{1}{\frac{2\pi}{N}b} \int_p^s \phi \, d\theta \quad (2)$$

According to that definition and using the Leibniz's rule, the following relation expresses the averaged derivative of some flow variable ϕ relative to some spatial variable s :

$$\frac{\partial \bar{\phi}}{\partial s} = \frac{1}{b} \frac{\partial b \bar{\phi}}{\partial s} - \frac{1}{\frac{2\pi}{N}b} \left[\phi \frac{\partial \theta}{\partial s} \right]_p^s \quad (3)$$

For compressible flows, the Favre average of some flow variable ϕ is introduced:

$$\tilde{\phi} = \frac{\int_p^s \rho \phi \, d\theta}{\int_p^s \rho \, d\theta} = \frac{\overline{\rho \phi}}{\bar{\rho}} \quad (4)$$

The perturbations of some variable ϕ compared to both averages are then defined:

$$\phi' = \phi - \bar{\phi} \quad \phi'' = \phi - \tilde{\phi} \quad (5)$$

Using these relations, the average of triple products appearing in the momentum and energy equations are deduced as:

$$\overline{\rho \phi \psi} = \bar{\rho} \tilde{\phi} \tilde{\psi} + \overline{\rho \phi'' \psi''} \quad (6)$$

The circumferentially-averaged set of equations is finally given by equations (7) to (9) and completed by the equation of state (10).

$$\frac{1}{b} \frac{\partial b \bar{\rho} \tilde{V}_j}{\partial s_j} = 0 \quad (7)$$

$$\frac{1}{b} \frac{\partial b \bar{\rho} \tilde{V}_i \tilde{V}_j}{\partial s_j} + \frac{1}{b} \frac{\partial b \bar{p}}{\partial s_j} \delta_{ij} = \frac{1}{b} \frac{\partial b \bar{\tau}_{ij}}{\partial s_j} - \frac{1}{b} \frac{\partial b \overline{\rho V_i'' V_j''}}{\partial s_j} + f_{bi} + f_{vi} \quad (8)$$

$$\frac{1}{b} \frac{\partial b \bar{\rho} \tilde{V}_j \tilde{H}}{\partial s_j} = \frac{1}{b} \frac{\partial b (\bar{\tau}_{ij} \tilde{V}_i - \bar{q}_j + \bar{\tau}_{ij}'' V_i'')}{\partial s_j} - \frac{1}{b} \frac{\partial b \overline{\rho V_j'' H''}}{\partial s_j} + e_b + e_v \quad (9)$$

$$\bar{P} = (\gamma - 1) \left[\bar{\rho} \tilde{E} - \frac{\bar{\rho} \tilde{V}_j \tilde{V}_j}{2} - \frac{\overline{\rho V_j'' V_j''}}{2} \right] \quad (10)$$

As mentioned previously, additional terms appear:

1. The inviscid and viscous blade forces f_{bi} and f_{vi} in the momentum equations and the viscous and inviscid energy source terms e_b and e_v in the energy equation. They appear as the result of the second term of the right-hand-side of equation (3), which physically represents the pressure, the shear stresses and the heat fluxes on the blade.
2. The circumferential stresses $\overline{\rho V_i'' V_j''}$ and the enthalpy correlations $\overline{\rho V_j'' H''}$. They represent respectively the transport of momentum and energy between the blade-to-blade and the axisymmetric flow fields.

The averaged flow state

This section is devoted to the procedure followed to compute the average flow field and the circumferential non-uniformities from the blade-to-blade calculation. First a 1D axial mesh (a meridian mesh) is generated with higher density at the leading and trailing edges to capture the rapid evolution of the flow in these regions. Circumferential arcs are generated for each node of this meridian grid to create the azimuthal one. Results from blade-to-blade computation are next interpolated on these nodes by bilinear interpolation in the blade-to-blade plane. The circumferential averaging is then performed on these arcs by integration with the trapezoidal rule, perturbations being next deduced and also averaged if needed.

The average kinetic energy² of the circumferential perturbations is defined as:

$$\bar{k} = \frac{\overline{\rho V_r'' V_r''} + \overline{\rho V_\theta'' V_\theta''} + \overline{\rho V_z'' V_z''}}{2\bar{p}} \quad (11)$$

As this kinetic energy contains some of the circumferential stresses, it is a good indicator of the difference between the blade-to-blade flow field and a solution uniform in the azimuthal direction. For this reason it is used in the following to quantify the level of circumferential non-uniformities.

Evolution of the ratio of this local average kinetic energy of circumferential perturbations to the local total average kinetic energy along the stage is depicted on figure 3.

The viscous and inviscid results are superimposed on this figure, even though they correspond to different blade loadings (see circumferential inviscid blade force on figure 4). Nevertheless, qualitative remarks can be made.

Firstly a peak of kinetic energy is located at the leading edge of the rotor. This increase of kinetic energy, that starts before the edge, is a potential effect due to the surrounding of the blade. The inviscid nature of this phenomenon is demonstrated by the shape of the inviscid curve. This zone of high fluctuations can also be noticed on figure 2 showing the relative Mach number contours in the blade-to-blade plane.

Secondly, the zone after the leading edge is still rich of fluctuations. It comes from the pressure load on the blade, as the circumferential force is mainly situated on the fore-part of the blade, as depicted on figure 4.

Fluctuations on the second half of the blades are driven by viscous effects, as the difference between both curves demonstrates. Actually the blade loading is much lower in this zone (figure 4) and the boundary layer develops on the blade walls. The fluctuations increase toward the trailing edge as the boundary layer develops.

²Radial velocity is kept for generality purpose but is zero since it is a blade-to-blade computation.

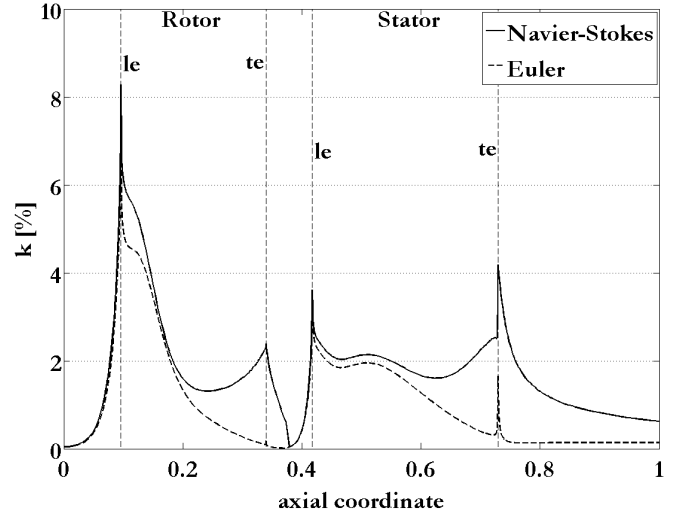


Figure 3. Axial evolution of the average kinetic energy of the circumferential perturbations \bar{k} in percent of the total kinetic energy: viscous (solid) and inviscid (dashed)

At the trailing edge a second peak is observed. It is due to the local reorganization of the flow coming from both sides of the blades. In the inviscid case, these fluctuations decrease rapidly to (nearly) zero. In the Navier-Stokes computation, the flow reorganization is followed by a viscous dissipation and a wake. This wake is visible on figure 2.

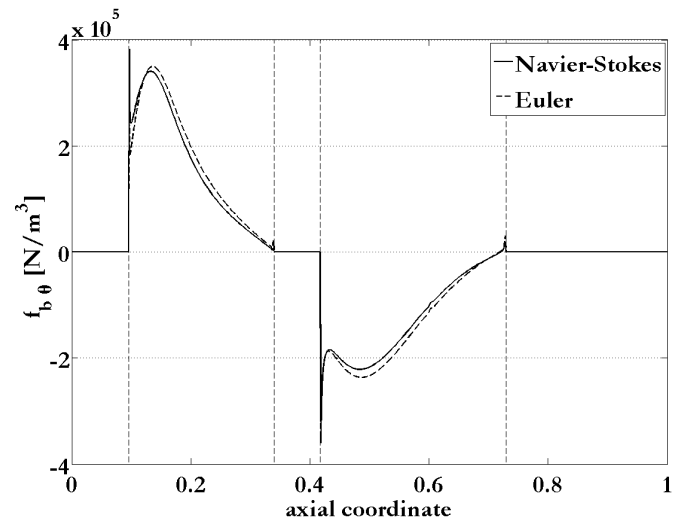


Figure 4. Axial evolution of the inviscid part of the circumferential blade force: viscous (solid) and inviscid (dashed) computations.

The location of the mixing plane is easily identifiable by the absence of circumferential non-uniformities.

In conclusion, if viscosity is important in the generation of circumferential fluctuations, the potential effects are also great contributors. This observation shows a major difference between circumferential and deterministic stresses. Actually, the latter take account for interactions between rows, interactions that come from large distance phenomena (such as wakes), which are mainly induced by viscosity.

The throughflow simulation tool

The throughflow code used for computations presented in this section solves the RANS equations circumferentially-averaged over a pitch, i.e. equations (7) to (9). The numerical method is based on an explicit time-marching cell-centered finite-volume approach.

The high order throughflow computation

In this section the contributions of the circumferential stresses are illustrated by introducing them into a throughflow simulation. To that end, correlations for the deviation and the losses are not used, as they involve some part of circumferential stresses resulting from the azimuthal average of the experimental data. This implies that all additional terms of equations (7) to (9) need to be extracted from the blade-to-blade simulation, i.e. the blade forces, the energy source terms and the circumferential stresses. Basically this means that pressure and viscous stresses on the blade walls are extracted in addition to circumferential stresses.

As the simulation is performed in the blade-to-blade plane, neither hub nor shroud are considered, which means that no end-wall boundary layers exist. Furthermore, the only viscous effect which is taken into account comes from the viscous blade force, i.e. no other blade-to-blade shear stress is included, which is an usual hypothesis in turbomachinery.

The figure 5 shows the axial evolution of the absolute Mach number (12) and the entropy (13) of the averaged flow field in four cases:

1. the blade-to-blade density averaged flow field
2. the throughflow simulation with inviscid blade force and energy source term (f_b, e_b)
3. the throughflow simulation with inviscid and viscous blade forces and energy source terms (f_b, f_v, e_b, e_v)
4. the throughflow simulation with all extra terms, including the circumferential stresses in addition to the preceding terms ($f_b, f_v, e_b, e_v, \overline{\rho V_i'' V_j''}, \overline{\rho V_j'' H''}$)

$$\tilde{M} = \frac{\tilde{V}}{\sqrt{\gamma R \tilde{T}}} \quad (12)$$

$$\tilde{s} = \frac{\gamma}{\gamma-1} R \ln(\tilde{T}) - R \ln(\tilde{P}) \quad (13)$$

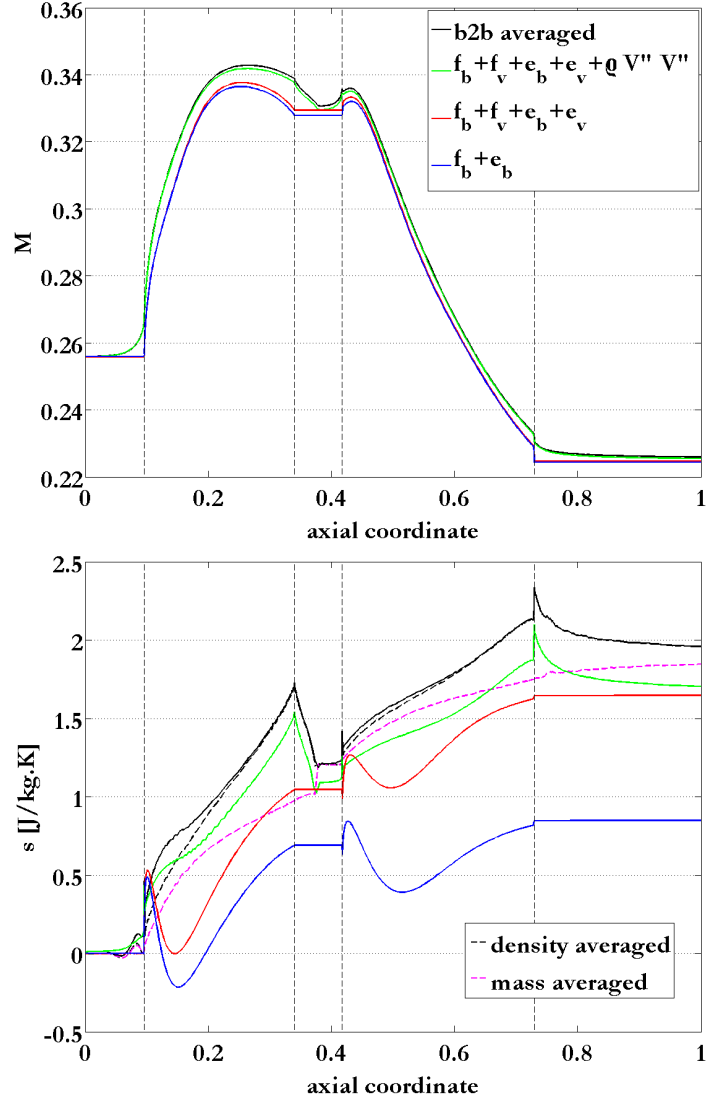


Figure 5. Axial evolution of the absolute Mach number (top) and the entropy (bottom) in four cases: 3D density averaged (black), $f_b + e_b$ (blue), $f_b + f_v + e_b + e_v$ (red) and $f_b + f_v + e_b + e_v + \overline{\rho V_i'' V_j''} + \overline{\rho V_j'' H''}$ (green)

A few remarks have to be made. The inviscid terms are responsible for the general structure of the flow field, as it was expected since they correspond to the main effect of the blades. The addition of the viscous terms translates the whole curve in the sense of an increase of losses, without modifying its shape. For both flow variables depicted, this curve is nearer the blade-to-blade averaged simulation than the previous one. For most of the flow variables, the last curve, that corresponds to the addition of the stresses, permits to fit quite well the blade-to-blade curve, by modifying locally the flow field. The evolution of the absolute Mach number is representative of this situation. The in-

provement of the description due to these last terms seems even larger than the one brought by the viscous terms.

More particularly, adding the stresses permits to take count of the potential effect before the leading edge. It also brings back the slow reorganization of the flow field after the trailing edge.

Concerning the entropy, one notices that the simulation does not approach so well the blade-to-blade averaged curve, even if the shape of the curve is captured. It happens as if a phenomenon growing slowly along the inner-blade channel was omitted. According to [12], this kind of behaviour could be due to the neglect of the blade-to-blade shear stresses. It is also probably due to some inaccuracies of the bi-linear interpolation performed to extract data from the blade-to-blade computation.

Furthermore, the nonuniform increase of entropy, that could seem to be unphysical, comes from the density averaging. The mass-averaged flow field is depicted (dashed magenta curve) for comparison and shows an expected behaviour. See [12] for more information. The mixing process is also noticeable by the entropy rise at the mixing-plane.

Finally a last curve is presented for the entropy evolution (dashed black curve). Actually this curve is the real density-average flow field, the previous so-called curve being based on mean quantities. The difference comes from the non-linearity of the relations used to reconstruct the quantities. For instance, the average of a *log* function is different from the *log* applied to the mean quantity (14), but that is the sole way to reconstruct flow variables with the available information. See [17] for more information.

$$\tilde{s} = \frac{\gamma}{\gamma-1} R \ln(\tilde{T}) - R \ln(\tilde{P}) \neq \frac{\gamma}{\gamma-1} R \ln(\tilde{T}) - R \ln(\tilde{P}) \quad (14)$$

In conclusion, introducing the circumferential stresses into a throughflow simulation is mandatory to fit the blade-to-blade averaged simulation.

THE HARMONIC ANALYSIS

In this section it is investigated whether an harmonic method is able to capture the circumferential stresses. To that end an harmonic reconstruction of the flow field, more particularly the blade-to-blade conservative variables ($\rho, \rho V_z, \rho V_\theta$ and ρE), is performed and analyzed.

First the frequency spectrum of the circumferential evolution of the flow field is detailed. Next a reconstruction of the circumferential stresses is performed. These approximated stresses are finally injected into a throughflow simulation which is compared to the computation run in the preceding section.

The local spectral analysis

The ability of Fourier series to reconstruct the circumferential evolution of the flow field at four sections A,B,C and D (see

table 2) is evaluated, in the viscous and inviscid cases. Even if circumferential non-uniformities are larger within the rotor, sections A, B, C and D have been chosen within the stator, as the aft-domain is longer. This permits to analyse the wake.

Section	Dimensionless axial coordinate
Inlet	0 %
Rotor le	10 %
Rotor te	34 %
Mixing-plane	38 %
Section A	40 %
Stator le	41 %
Section B	42 %
Section C	69 %
Stator te	73 %
Section D	87 %
Outlet	100 %

Table 2. Main sections of the stage in dimensionless axial coordinate.

Figure 6 presents the circumferential perturbations over ρV_z (top) and ρV_θ (bottom) at sections A, B, C and D. Higher perturbations are observed at stations B and C, i.e. in the inner-blade passage. This is in accordance with figure 3 depicting the kinetic energy of the circumferential perturbations and the fact that the blades are the generators of non-uniformities.

Furthermore the differences between these two stations and sections A and D are also remarkable. Due to the no-slip conditions on the blade walls, the perturbations are equal to minus the mean flow field at those locations to set the blade-to-blade velocity field to zero. On the contrary, the flow at section A is only directed by potential effects, i.e Euler-type phenomena, while station D is affected by the wake.

It is well known that a Fourier series converges to the exact function provided that it is piecewise continuous and periodic. This last condition is not fulfilled in a bladed passage, as the flow field on the pressure and suction sides is in general different. This means that in order to compute a Fourier series in the blade passage, one has to artificially make the function periodic. The main drawback is that by doing so, the real evolution is altered. Hence a special care must be taken to make the function periodic with minimal modification of its frequency spectrum. There are many ways to extend the function. Two simple solutions are presented hereafter.

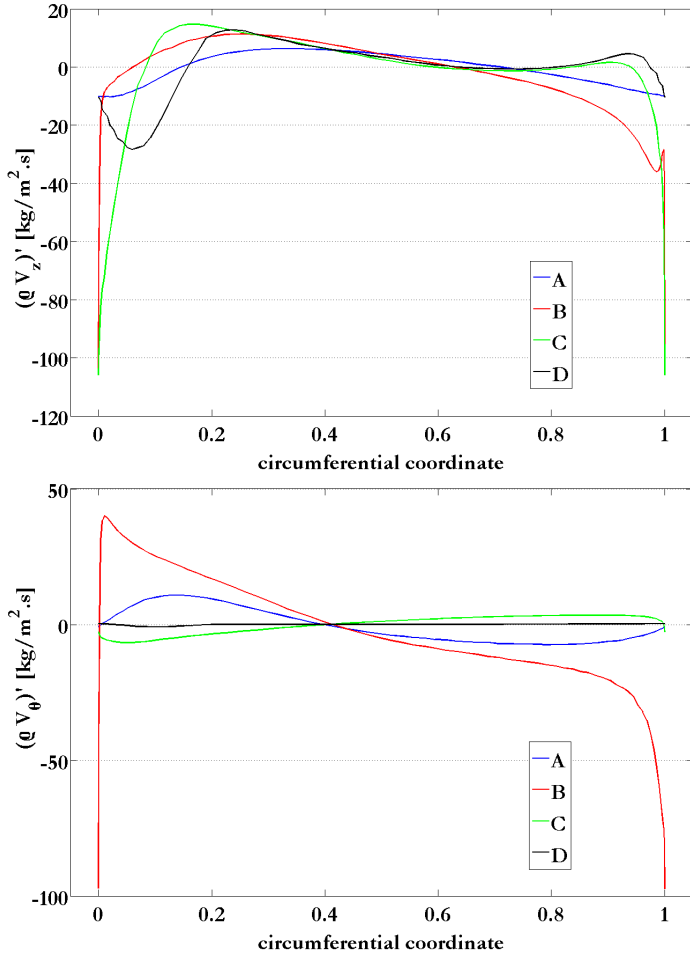


Figure 6. Circumferential perturbations over ρV_z (top) and ρV_θ (bottom) at sections A (blue), B (red), C (green) and D (black)

A linear prolongation is used in case of viscous simulation. Due to the boundary layers on both sides of the blades, the evolution of the conservative variables are already nearly periodic³ (see figure 6), with sharp variations at both ends of the circumferential domain (the inner-blade channel). Hence it is sufficient to add a small linear portion of curve to make the signal periodic with a piecewise extension. The result is depicted on figure 7, top.

For inviscid simulations this kind of extension is too sharp and leads to unphysical oscillations and to distortion of the signal (see figure 7, bottom). The solution is to mirror the existent function. As it prolongs the signal by itself, a piecewise variation is obtained in case of initial smooth evolution, and does not introduce extra spectral behaviour⁴ (see figure 7, bottom).

³Actually evolutions of $(\rho V_z)'$ and $(\rho V_\theta)'$ are periodic due to the no-slip condition, but not ρ' and $(\rho E)'$.

⁴For viscous simulations, this extension is not efficient because it is equivalent to double a "nearly" periodic signal, which "nearly" makes half of the harmonics unnecessary, hence leading to a slower convergence (see figure 7, top).

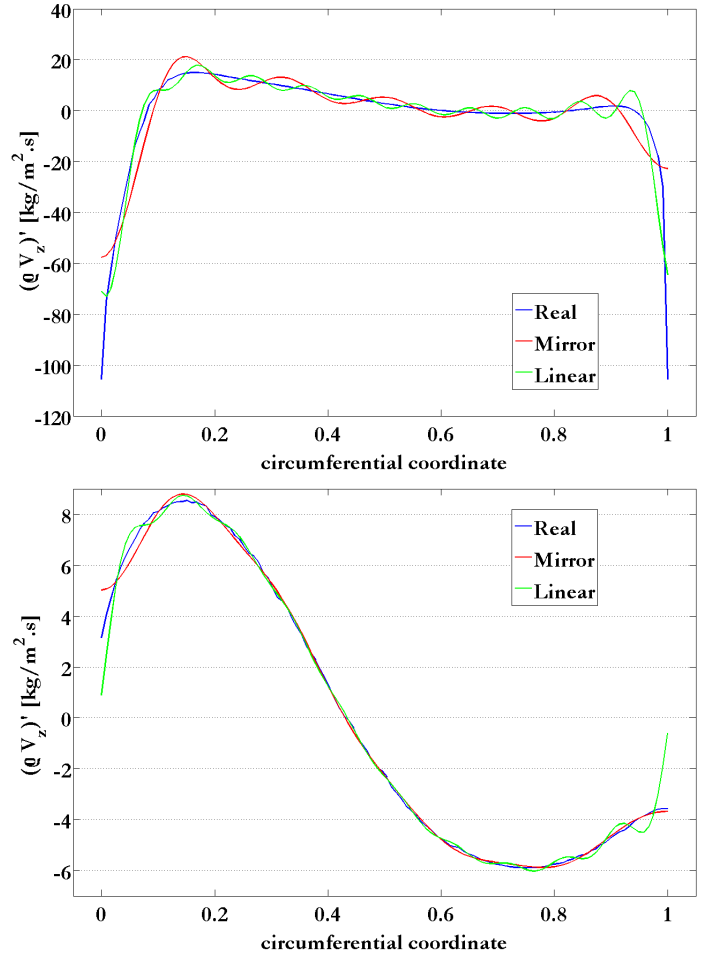


Figure 7. Harmonic reconstruction of circumferential evolution of $(\rho V_z)'$ with 10 modes in case of viscous (top) and inviscid (bottom) computations. Real function (blue), Fourier series with mirror extension (red) and linear extension (green).

In what follows, the linear extension is used systematically for viscous computations, while the mirror prolongation is used for inviscid ones.

Other methods such as smooth extension by polynomial functions are other possibilities, but they would perturb the low-frequency part of the spectrum by including their own frequency behaviour.

Figure 8 presents the logarithm of the absolute value of the Fourier coefficients divided by the first one for $(\rho V_z)'$ (top) and $(\rho V_\theta)'$ (bottom), what will be called the frequency spectrum. The section A appears to be quite poor in terms of spectral content, what was expected since this region is driven by potential effects. This kind of behaviour is also remarkable at section D, of which location is in the wake. Hence the same conclusion holds for outer-blade viscous effects. Noticing that the level of spectral decrease from the fourth mode is the same for both sections, one

can conclude that this kind of evolution is characteristic of outer-blade flow field for which first modes dominate the description. Concerning the right part of the spectrum for both sections, the high frequency terms of small amplitude probably render of some noise. The latter is due to the simple bilinear interpolation used to obtain the circumferential evolution of the flow field from the blade-to-blade computation.

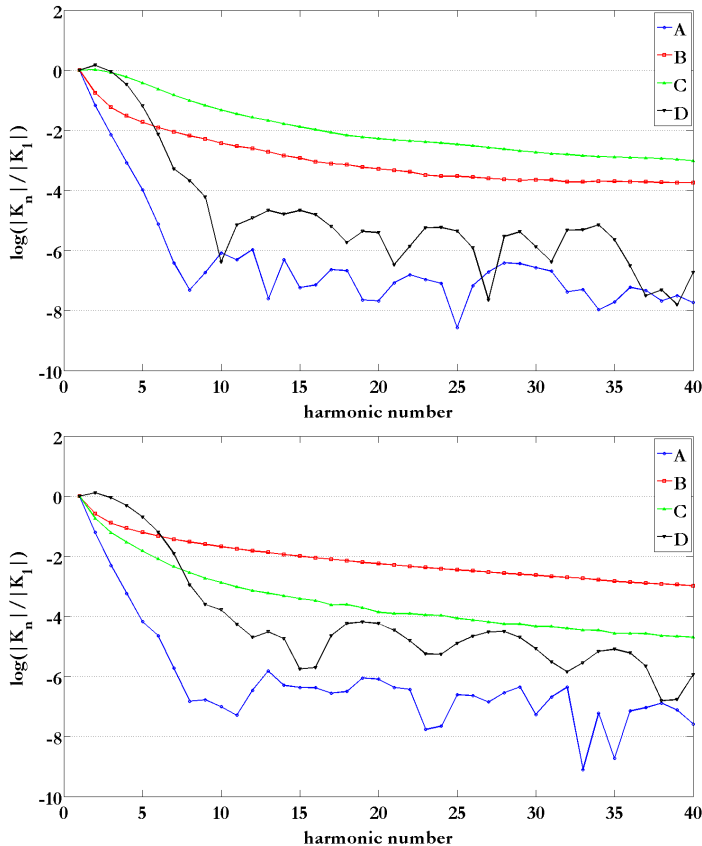


Figure 8. Frequency spectrum of $(\rho V_z)'$ (top) and $(\rho V_\theta)'$ (bottom) at sections A (blue), B (red), C (green) and D (black)

On the contrary, sections B and C are rich in terms of spectral content. The reduction of the Fourier coefficients is lower, which demonstrates that high frequency phenomena characterize the flow field at those locations in addition to low frequency ones. Both sections correspond to inner-blade flow field, one near the leading edge (section B) and the other one near the trailing edge (section C). Hence both locations involve viscous boundary layer frequency spectrum, that corresponds to the same low reduction of Fourier coefficients.

This example shows a strong difference between inner-blade and outer-blade regions and indicates the need for a more costly reconstruction inside the blade passage, characterized by a larger range of length scales.

Furthermore, the comparison of the spectra corresponding to $(\rho V_z)'$ and $(\rho V_\theta)'$ shows that the convergence is different depending on the conservative flow variable. For instance, the level of reduction of the Fourier coefficients at section B is higher for $(\rho V_z)'$ than for $(\rho V_\theta)'$. The opposite behaviour is noticed at section C. This means that even though a uniform convergence can be expected, the level will probably be different for the various flow variables, depending on the convergence of the most influent circumferential stress.

This difference of convergence properties does not appear at sections A and D, the latter being richer due to the wake.

The harmonic reconstruction

In this section the difficulty of reconstructing circumferential stresses characterized by a large frequency spectrum is investigated, particularly for the inner-blade zone. To that end, the blade-to-blade evolution of the flow field is reconstructed by Fourier series along the whole stage, for different numbers of modes. The qualities of reconstruction in case of viscous and inviscid computations are also compared.

Figure 9 depicts the kinetic energy of the circumferential non-uniformities corresponding to an harmonic reconstruction of the flow field and the ratio of this reconstructed kinetic energy for 1, 3, 5, 10, 20 and 50 modes to the real one. The convergence of the kinetic energy appears to be uniform and the general shape of the axial evolution is captured since the first mode. Hence using more modes for the reconstruction is always rewarded. It is a consequence of the uniform convergence of the Fourier series of the conservative variables.

Another noticeable fact is the large contribution of the first modes to the reconstruction, as it has already been observed in the previous section, particularly for outer-blade field. The real evolution is nearly captured with only 5 modes. Knowing that deterministic stresses are partly characterized by such circumferential evolutions, this explains why few modes are enough to take into account interactions between rows.

On the contrary, as it was expected according to figure 8, the convergence is much lower for the inner-blade field. Hence if 10 modes permit to capture about 90 % of the kinetic energy, 50 modes are not enough to fit the real evolution.

Figure 9 (bottom) also addresses the difference of convergence between the leading edge and the trailing edge regions. For few modes, the error on the kinetic energy is lower in the leading edge area. Actually first harmonics can only capture circumferential evolutions characterized by large length variations. This means that first modes miss the boundary layer. Thus, near the leading edge, as the boundary layer is still very thin, the error committed on the circumferential stresses by neglecting this local evolution is lower than the one committed by omitting a thicker boundary layer near the trailing edge (see figure 6, top).

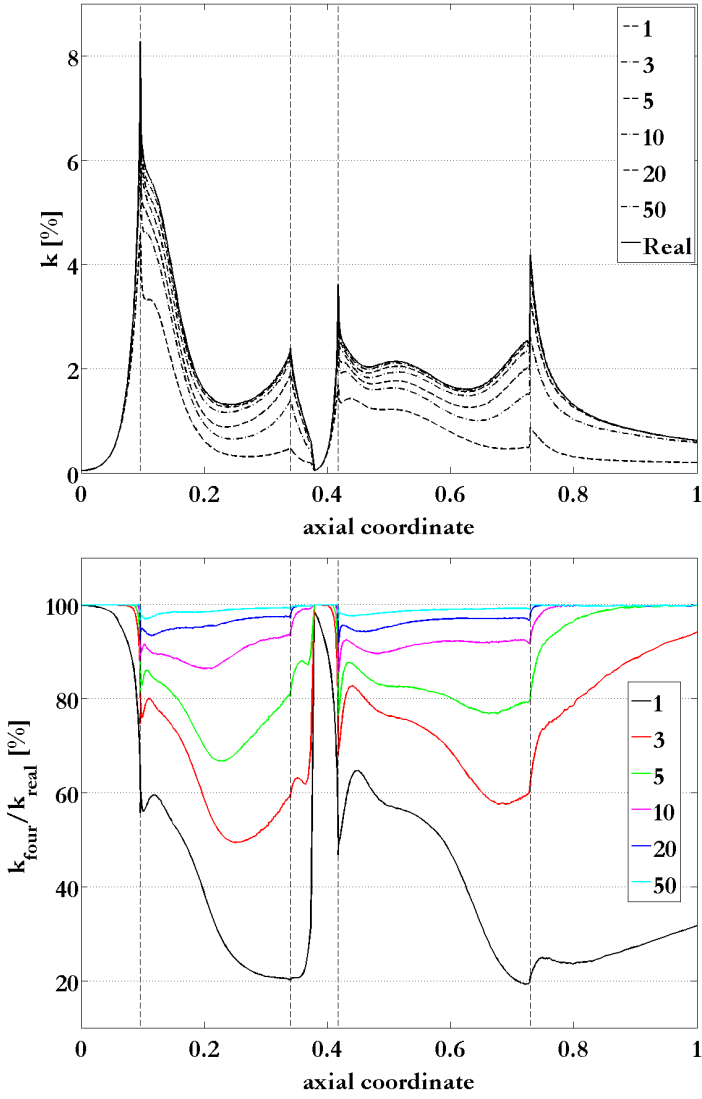


Figure 9. Kinetic energy (top) after harmonic reconstruction for 1, 3, 5, 10, 20 and 50 modes (dashed) compared to exact one (solid) and ratio of reconstructed field kinetic energy over real field one (bottom).

For larger number of harmonics the situation inverts. From 10 modes, the relative error is larger in the leading edge region. For higher harmonics, the capture of the boundary layer really starts (see top figure 7). Hence the quality of the approximation depends on the ability of the series to follow the evolution of the field near the walls. As the boundary layer is thinner near the leading edge, more harmonics are needed than in the trailing edge region. According to [19], the number of harmonics mandatory to fit the evolution in a boundary layer of thickness ϵ ($\ll 1$) is proportional to $1/\sqrt{\epsilon}$ for an unevenly spaced Chebyshev interpolation grid⁵. This kind of grid is used here.

⁵A Chebyshev grid is a cosinusoidal distribution of points, i.e. more closely spaced near the walls.

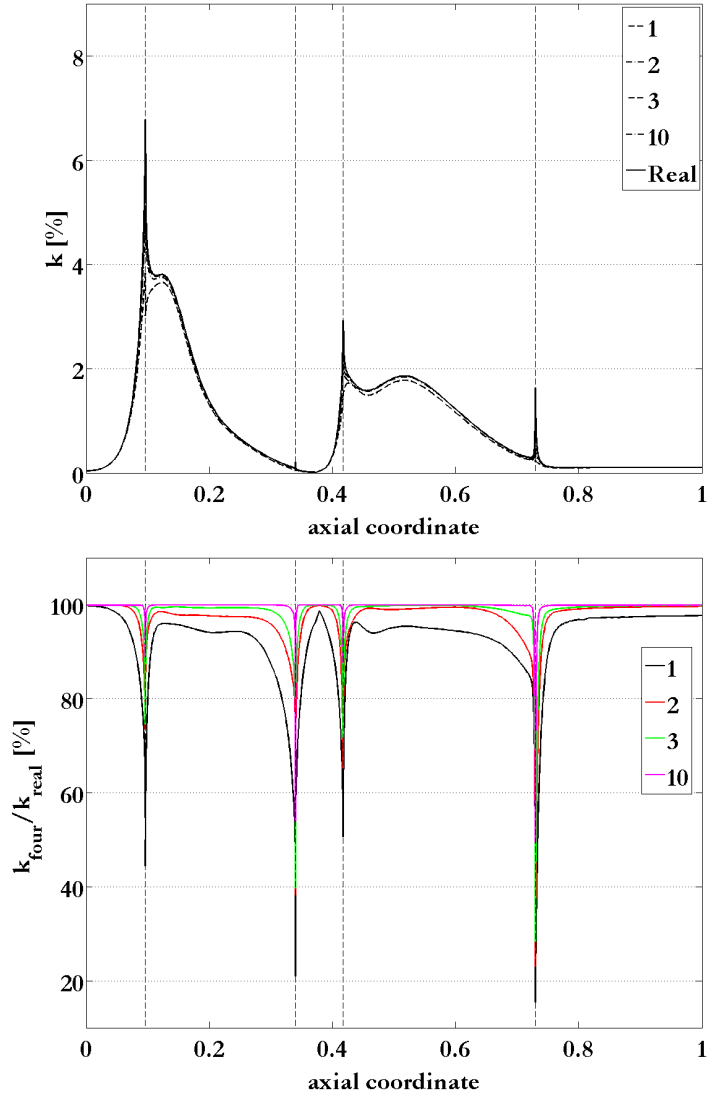


Figure 10. Kinetic energy (top) after harmonic reconstruction for 1, 2, 3 and 10 modes and ratio of reconstructed field kinetic energy over real field one (bottom).

Finally the same procedure for the inviscid computation is summarised on figure 10 for 1, 2, 3 and 10 modes. In this case, the flow field is characterized by large lengths, i.e. low frequencies. That is why the convergence is so fast, 3 modes leading to more than 95 % everywhere apart from the leading edge and trailing edge regions where higher frequency phenomena exist.

This last example confirms the split of the frequency spectrum into two regions: the first one, about the first three modes, corresponding to potential effects and about two third of the perturbation field intensity and the second one to localized viscous behaviours.

The harmonic throughflow closure

In this last section the reconstructed circumferential stresses are injected into the throughflow code, according to the same procedure as already used for real ones. This will verify the ability of the harmonic method to reproduce the physical evolution of the field detailed in a preceding section.

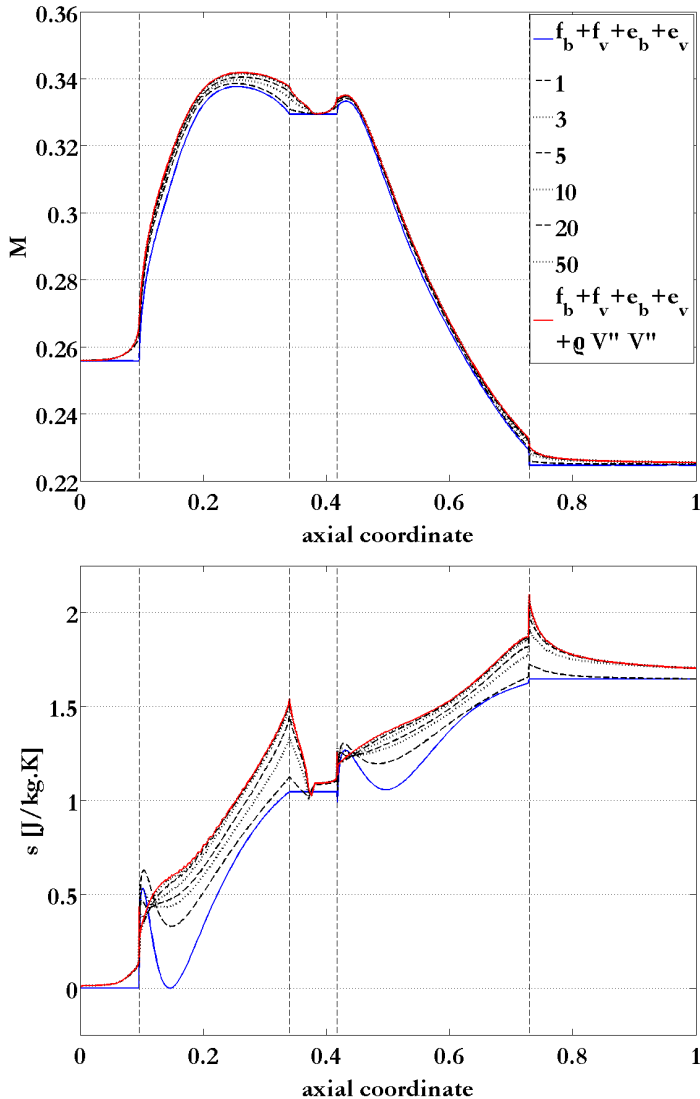


Figure 11. Axial evolution of the absolute Mach number (top) and the entropy (bottom). Intermediates curves correspond to 1, 3, 5, 10, 20 and 50 harmonics used to reconstruct the field.

Figure 11 illustrates the axial evolution of the absolute Mach number (top) and the entropy (bottom) of the averaged flow field for several qualities of harmonic reconstructions. This figure confirms that few modes are enough to reproduce the adaptation

close to the blade. As expected, the convergence in the inner-blade passage is slower. Nevertheless, the curves demonstrate that the shape is progressively transforming to fit the “exact” curve, leading to the conclusion that the shape-convergence is uniform.

To quantify the level of convergence of the field, an average error operator is introduced. ϕ_{100} stands for a primitive field variable computed with the throughflow fed with inviscid and viscous source terms. ϕ_0 is its counterpart computed with exact circumferential stresses added and ϕ is the same variable corresponding to reconstructed circumferential stresses. The error is defined by expression (15) for a sample of S axial nodes.

$$\text{error} = \sqrt{\frac{\sum_{k=1}^S (\phi_k - \phi_{0k})^2}{\sum_{k=1}^S (\phi_{100k} - \phi_{0k})^2}} \quad (15)$$

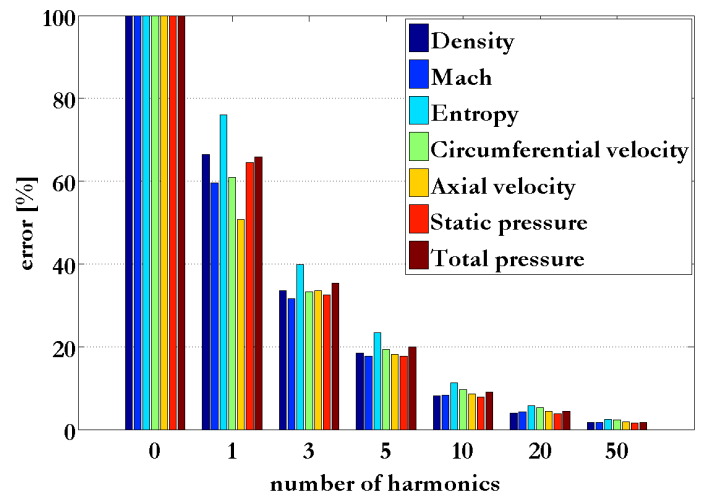


Figure 12. Relative error on some flow variables resulting from a throughflow computation fed with $f_b + f_v + e_b + e_v$ plus the circumferential stresses reconstructed with 0, 1, 3, 5, 10, 20 and 50 modes.

The resulting relative error is depicted on figure 12 for some flow variables, which confirms the uniform convergence. This figure shows also the difference of sensitivity of the flow variables to the number of harmonics used to reconstruct the flow field. It has probably two origins. First, since the various flow variables are reconstructed with different combinations of the conservative variables, the combinations of approximation errors differ also. The second one comes from the different levels of spectral convergence of the conservative variables (see figure 8), as mentioned previously. The latter implies that the various

circumferential stresses do not have the same quality of approximation. This passes on to the flow variables, depending on the most influent stress for each one. Nevertheless, one can say that all variables have a comparable relative error level. Finally, as it has been noticed for the kinetic energy, the precision rapidly increases, leading to an error of about 10 % for 10 modes.

One could question whether this kind of convergence is a general result. According to the authors, a positive answer cannot be far from the reality for the following reason. Two extreme characteristic lengths have been under examination: large lengths from potential effects and small ones from boundary layers. Hence this frequency spectrum covers most of the non-examined sources of non-uniformities (spanwise mixing, corner stall,...), except the shocks for which nothing can be concluded.

CONCLUSION

The objective of this contribution was to demonstrate the ability of an harmonic reconstruction to bring back the mean effect of circumferential non-uniformities in a throughflow simulation.

This was done in several steps. Firstly the interest of circumferential stresses was highlighted by extracting them from a blade-to-blade simulation and by injecting them into a throughflow code. It was in particular illustrated that the flow adaptation was brought back by these terms. Effects could be much larger in presence of endwalls, as presented in [12].

The frequency spectrum of the field was next detailed in four representative sections, highlighting the difference between inner-blade and outer-blade fields.

The reconstruction of the flow field further illustrated a uniform convergence of the circumferential stresses with the number of harmonics and a rapid axial shape capture. The rapid convergence of the outer-blade field was also stressed, explaining why interactions between rows are well approximated with few harmonics in unsteady non-linear harmonic methods.

The last throughflow computation with reconstructed circumferential stresses demonstrated that the convergence rate on flow variables is the same as the one on circumferential stresses, leading to the conclusion that each additional harmonic used is rewarded.

Hence this contribution allows to envisage extending the efficient harmonic method to throughflow simulation. This method could be as efficient as the unsteady one in case of inviscid computation. It will probably be more costly for viscous simulations due to the larger frequency spectrum of circumferential non-uniformities. As a remedy one could question whether other types of functions than trigonometric ones would better fit azimuthal evolutions in the viscous cases, maybe the wavelets functions that are able to reproduce sharp variations.

One must nevertheless admits that in this contribution, additional terms such as blade forces and energy source terms were

supposed known and exact. It will be mandatory to find a way of computing them without the recourse to empirical correlations to have an efficient calculation tool. Some possibilities are proposed in [12].

Future work is planned to adapt the harmonic method to throughflow simulation and to test implementation of this one in a throughflow simulation tool.

ACKNOWLEDGEMENTS

The author would like to thank Jean-François Simon for the time spared in discussions about the throughflow modeling and for his useful remarks.

REFERENCES

- [1] Adamczyk, J.J., 1984, *Model Equation for Simulating Fows in Multistage Turbomachinery*, NASA-TM-86869.
- [2] Adamczyk, J.J., Mulac, R.A., Celestina, M. L., 1986, *A Model for Closing the Inviscid Form of the Average-Passage Equation System*, Transactions of the ASME Journal of Turbomachinery, vol. 108, pp. 180-186.
- [3] He, L., Ning, W., 1998, *Efficient Approach for Analysis of Unsteady Viscous Flows in Turbomachines*, AIAA journal, vol. 36, pp. 2005-2012.
- [4] Chen, T., Vasanthakumar, P., He, L., 2001, *Analysis of Unsteady Blade Row Interaction Using Nonlinear Harmonic Approach*, AIAA journal of Propulsion and Power, vol. 17, pp. 651-658.
- [5] Stridh, M., Eriksson, L.E., 2005, *Modeling Unsteady Flow Effects in a 3D Transonic Compressor*, ASME Paper GT2005-68149.
- [6] Vilmin, S., Lorrain, S., Hirsch, C., Swoboda, S., 2006, *Unsteady Flow Modeling Across The Rotor/Stator Interface Using The Nonlinear Harmonic Method*, ASME Paper GT2006-90210.
- [7] Hall, K.C., Thomas, J.P., Clark, W.S., 2002, *Computation of Unsteady Nonlinear Flows in Cascades Using a Harmonic Balance Technique*, AIAA Journal, vol. 40, No. 5, pp. 879-886.
- [8] Smith, L.H., 1966, *The Radial-Equilibrium Equation of Turbomachinery*, Transactions of the ASME Journal of Engineering for Power, Series A, Vol. 88, pp. 1-12.
- [9] Sehra, A.K., Kerrebrock, J.L., 1979, *Blade-to-Blade Effects on Mean Flow in Transonic Compressors*, AIAA Journal, vol. 19, No. 4, pp. 476-483.
- [10] Jennions, I.K., Stow, P., 1986, *The Importance of Circumferential Non-uniformities in a Passage-Averaged Quasi-Three-Dimensional Turbomachinery Design System*, Transactions of the ASME Journal of Engineering for Power, vol. 108, pp. 240-245.

- [11] Perrin, G., Leboeuf, F., 1995, *Investigation of Throughflow Hypothesis in a Turbine Cascade Using a Three-Dimensional Navier-Stokes Computation*, Transactions of the ASME Journal of Turbomachinery, vol. 117, pp. 126-132.
- [12] Simon, J.F., 2007, *Contribution to Throughflow Modelling for Axial Flow Turbomachines*, Ph.D thesis, University of Liège.
- [13] Adkins, G.G. Jr, Smith, L.H. Jr, 1982, *Spanwise Mixing in Axial-Flow Turbomachines*, Transactions of the ASME Journal of Engineering for Power, vol. 104, pp. 97-110.
- [14] Gallimore, S.J., Cumpsty, N.A., 1986, *Spanwise Mixing in Multistage Axial Flow Compressors: Part I - Experimental Investigation*, Transactions of the ASME Journal of Turbomachinery, vol. 108, pp. 2-9.
- [15] Roberts, W.B., Serovy, G.K., Sandercock, D.M., 1986, *Modeling the 3-D Flow Effects on Deviation Angle for Axial Compressor Middle Stages*, Transactions of the ASME Journal of Engineering for Gas Turbines and Power, vol. 108, pp. 131-137.
- [16] Çetin, M., Üçer, A.Ş., Hirsch, C., Serovy, G.K., 1987, *Application of Modified Loss and Deviation Correlations to Transonic Axial Compressors*, AGARD R-745.
- [17] Bardoux, F., 2000, *Modélisation des interactions instationnaires rotor-stator en turbomachine multi-étages*, Ph.D thesis, Ecole centrale de Lyon.
- [18] Spiegel, M.R., 1968, *Schaum's Mathematical Handbook of Formulas and Tables*, Mc Graw Hill.
- [19] Boyd, J.P., 2001, *Chebyshev and Fourier spectral methods*, 2nd edition, Dover, New-York.